Stanford Exploration Project, Report 77, November 17, 1997, pages 1–226

Stanford Exploration Project, Report 77, November 17, 1997, pages 1–226

Angle-dependent reflectivity estimation

David E. Lumley[1]

keywords: *amplitudes, reflectivity, modeling, prestack, phase, least squares*

ABSTRACT

I derive an analytical least-squares inverse solution to the problem of estimating angle-dependent reflectivity from prestack seismic reflection data. The reflection coefficients *and* the reflection angles are estimated simultaneously directly from the prestack seismic reflection data, without a priori knowledge of geologic structure or dip. I define a forward theory which relates angle-dependent reflection data to a generalized reflectivity model combining elements of Zoeppritz plane wave reflection and Rayleigh-Sommerfeld diffraction. The l_2 inverse solutions for reflectivity and reflection angle are then derived by a standard application of stationary phase and Gauss-Newton gradient optimization, and naturally incorporate l_2 compensation for limited data acquisition aperture, source and receiver directivity, geometric spreading, transmission loss, and high-frequency intrinsic Q attenuation. Uncompensated reflectivity amplitude errors include coherent noise (e.g., multiples, surface waves, etc.), steep-dip operator spatial aliasing, migration velocity error, and data mute zones. The method is validated on a synthetic data example in the presence of dips up to 30 degrees, and should prove to be a useful component of seismic prestack amplitude analysis (AVO) and impedance inversion.

INTRODUCTION

Estimation of angle-dependent reflectivity is a critical step in the larger inverse problem of mapping subsurface material properties from surface seismic reflection data (e.g., Lumley and Beydoun, 1991). The latter is, in turn, important for hydrocarbon exploration and detection, and crucial for reservoir characterization and management.

Bleistein (1987) addressed this problem based on the work of Beylkin (1985). By a suitable choice of a Kirchhoff integrand, Bleistein was able to show that his trial solution reduced to an estimate of angle-dependent reflectivity under the stationary phase approximation. However, it is not clear that the solution is robust in the sense of an l_p-norm estimate, nor that it can be derived in a straightforward inverse theory

[1]**email:** not available

approach, starting with some assumed forward model for reflection and diffraction. More recently, de Bruin (1992) and Cunha (1992) approached this problem from a finite-difference perspective. de Bruin estimates angle-dependent reflectivity using an w-x migration scheme. However, de Bruin processes the data in constant ray parameter sections, and so cannot estimate the reflection angles directly from the data, without a posteriori information on the structure and dip. His second-pass procedure of evaluating the reflection angles after picking migrated reflector horizons may represent an inefficient and unstable process. Cunha (1992) applied a reverse-time migration procedure to estimate angle-dependent reflectivity. As with de Bruin, Cunha needs to invoke and evaluate a set of new imaging conditions to estimate reflectivity, but, unlike de Bruin, Cunha is able to directly estimate reflection angles from the data. Possible disadvantages to Cunha's method are its prohibitive computational expense, and its potential for instability due to its formulation in the common-shot domain.

In this paper I derive a robust least-squares estimate of angle-dependent reflectivity, starting from a Rayleigh-Sommerfeld diffraction-reflection model, and a straightforward application of least-squares inverse theory. The method does not require the definition of any particular imaging conditions, and both reflectivity and reflection angle are directly estimated from the data without a priori knowledge of structural dip. The results are seen to be extensions to Bleistein's solutions, and cost little more than a standard Kirchhoff prestack migration to implement.

This paper proceeds as follows. I first define a forward model relating angle-dependent seismic reflection data to a generalized reflection model which combines elements of Zoeppritz plane-wave reflection and Rayleigh-Sommerfeld diffraction. On the basis of this forward model, I formulate a least-squares inverse problem to estimate the angle-dependent reflection coefficient as a function of subsurface coordinate and offset. This analysis leads to two coupled normal equations for reflectivity and reflection angle, as a function of the recorded seismic data. I decouple the two equations using a stationary phase approximation. I then solve the reflectivity equation using a standard Gauss-Newton gradient optimization technique, and approximate the reflection angle solution with an analogous expression, based on a physically intuitive approach.

THEORY

Forward problem

To begin, I define a forward model for a "generalized" PP reflectivity, R_{PP}, which combines elements of Zoeppritz plane wave reflection (e.g., Aki and Richards, 1980), and Rayleigh-Sommerfeld diffraction (e.g., Goodman, 1968). I define a differential volume element R_{PP} as

$$R_{PP} = \frac{iw}{\alpha} \grave{P}\acute{P} \cos\phi_s \cos\phi_r \ , \tag{1}$$

for $|\phi_s, \phi_r| \leq \pi/2$, and zero otherwise. Here, w is angular frequency, α is compressional velocity, $\grave{P}\acute{P}$ is the Zoeppritz PP plane wave reflection coefficient and ϕ_s (ϕ_r) is the angle between the incident source (receiver) ray and the specular ray in Figure **??**. The specular ray is defined as the reflection raypath for which the incident angle Θ is equal to the angle of reflection, with respect to the normal to the reflecting surface. The specular angle Θ is related to ϕ_s and ϕ_r in that $\Theta = |\theta_s - \phi_s| = |\theta_r - \phi_r|$, where θ_s is the angle between an arbitrary source ray and the reflector normal, and θ_r is the angle between an arbitrary receiver ray and the reflector normal. Frazer and Sen (1985, eqn. 9b) derive an analogous expression to (1) for elastic Kirchhoff-Helmholtz surface integrals.

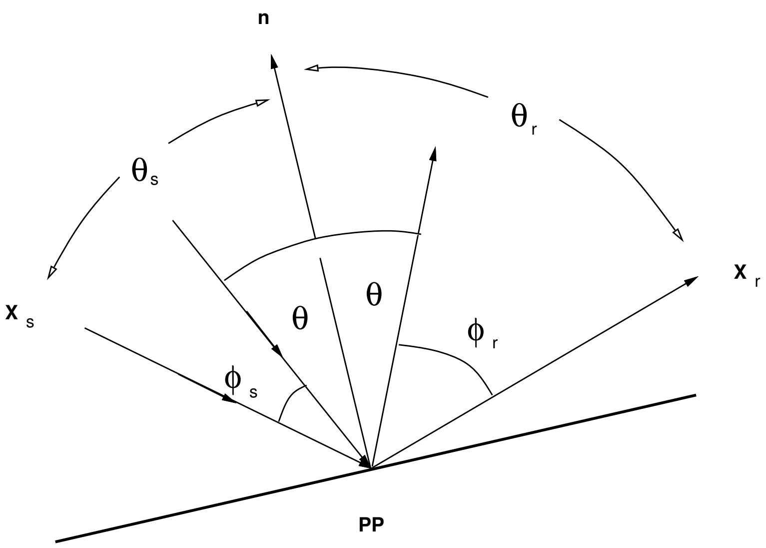

Figure 1: Ray geometry for generalized reflection and diffraction. $\boxed{\text{david2-geom}}$ [NR]

Equation (1) can be integrated over the subsurface volume to forward model the reflected scalar wavefield:

$$U(\mathbf{x}_r, \mathbf{x}_s, w) = \int_V A_s A_r R_{PP} e^{iw\tau} dV \ , \tag{2}$$

where $\mathbf{x}_s$ ($\mathbf{x}_r$) is the shot (receiver) coordinate, and τ is the total traveltime from source to reflection point to receiver. A_s (A_r) is the WKBJ amplitude factor along the source (receiver) leg of the raypath to the subsurface reflection point $\mathbf{x}$, and incorporates the amplitude effects of source (receiver) directivity, geometric spreading, transmission loss, and intrinsic high-frequency Q attenuation. All of these quantities are readily available by raytracing through the background migration velocity model.

The scalar U may be the wave pressure measured in a hydrophone, the magnitude of the displacement vector measured at a geophone, or an individual (e.g. vertical) component of the displacement vector if the appropriate component directivity is introduced into A_r.

It is important to note that the volume integration (2) models a single trace for any arbitrary source and receiver location. There is no "preferred" acquisition geometry for this synthesis; it works for shot gathers as well as random trace orientations. In particular, (2) is perfectly adequate for *constant offset* survey data, which will be the focus of this work.

Inverse problem

The least-squares inverse problem is formulated as follows. Consider our observations consist of a set of constant offset data $D(\mathbf{x}_m;\mathbf{x}_h,w)$. A constant-offset l_2 misfit energy functional can be defined as

$$E(\mathbf{x}_h) = \int_w \int_{\mathbf{x}_m} \left[D(\mathbf{x}_m;\mathbf{x}_h,w) - U(\mathbf{x}_m;\mathbf{x}_h,w)\right]^2 \, d\mathbf{x}_m \, dw \ , \tag{3}$$

Minimizing (3) with respect to $\grave{P}\acute{P}$ and the specular angle Θ leads to two coupled normal equations:

$$\frac{\partial E}{\partial \grave{P}\acute{P}} = -2 \int_w \int_{\mathbf{x}_m} [D-U] \left[\int_V ik\, A_s A_r \cos\phi_s \cos\phi_r e^{iw\tau} dV\right] \, d\mathbf{x}_m \, dw \ , \tag{4}$$

where $k = w/\alpha$ is the spatial wavenumber, and

$$\frac{\partial E}{\partial \Theta} = -2 \int_w \int_{\mathbf{x}_m} [D-U] \left[\int_V ik\, A_s A_r \grave{P}\acute{P} \left(\cos\phi_s \sin\phi_r + \sin\phi_s \cos\phi_r\right) e^{iw\tau} dV\right] \, d\mathbf{x}_m \, dw \ . \tag{5}$$

In general, these two coupled equations should be solved simultaneously for $\grave{P}\acute{P}$ and Θ. As that is rather complicated, for now I will present a much simpler approximate approach. The equations can be *decoupled* by the stationary phase (high-frequency) approximation, in which the major contribution to (2) occurs near the specular point when $\phi_s \approx \phi_r \approx 0$. In this case, the $\grave{P}\acute{P}$ equation can be solved independently of Θ, and the result can be backsubstituted into the original normal equation for Θ. It is important to note that by assuming the *generalized* form of diffraction-reflection in (1), I have derived *two* equations, one for each of $\grave{P}\acute{P}$ and Θ. Now I will proceed to solve only the $\grave{P}\acute{P}$ equation under stationary phase, and use the $\grave{P}\acute{P}$ result to solve the Θ equation. Had I *started* with the assumption of specular reflection (stationary phase), I would have had only one equation for *specular* $\grave{P}\acute{P}$, and no equation describing Θ. That is a very important distinction.

The first step in the decoupling is to apply the method of stationary phase to the volume integral within the misfit error functional E of (3). The phase component γ of the volume integral is

$$\gamma(\mathbf{x};\mathbf{x}_s,\mathbf{x}_r) = w\tau(\mathbf{x};\mathbf{x}_s,\mathbf{x}_r) = w\left[\tau_s(\mathbf{x};\mathbf{x}_s) + \tau_r(\mathbf{x};\mathbf{x}_r)\right] \ . \tag{6}$$

The stationary point of the phase with respect to the integration variable $\mathbf{x}$ is defined by the equation:

$$\nabla\gamma = w\nabla\tau = w(\nabla\tau_s + \nabla\tau_r) = 0 \ . \tag{7}$$

In particular,

$$\nabla\tau_s(\mathbf{x})\cdot\mathbf{n}(\mathbf{x}) = -\nabla\tau_r(\mathbf{x})\cdot\mathbf{n}(\mathbf{x}) \ , \tag{8}$$

where $\mathbf{n}$ is the normal to the reflecting surface at the point $\mathbf{x}$. The stationary condition (8) is equivalent to:

$$\cos\theta_s(\mathbf{x}) = \cos\theta_r(\mathbf{x}) \ , \tag{9}$$

which in turn is simply stating the law of specular reflection for a $\grave{P}\acute{P}$ wave at a reflecting boundary. In other words, the stationary point, and hence the major contribution to the integral of the misfit error functional, occurs at the condition of specular reflection, when $\phi_s \approx \phi_r \approx 0$. In this case, the misfit error at stationarity reduces to:

$$E(\mathbf{x}_h) = \int_w \int_{\mathbf{x}_m} \left[D(\mathbf{x}_m;\mathbf{x}_h,w) - \int_V ik\, A_s A_r \grave{P}\acute{P} e^{iw\tau}\, dV\right]^2 d\mathbf{x}_m\, dw \ . \tag{10}$$

Now the error misfit functional (10) is in standard linear form, and can be solved for $\grave{P}\acute{P}$ with a traditional Gauss-Newton gradient optimization method. The solution for $\grave{P}\acute{P}$ should then be backsubstituted into the Θ normal equation, and this decoupling should lead to an l_2 solution for Θ, which would not have been otherwise possible had we *started* directly with the specular form (10).

Reflectivity

Under the stationary phase approximation, the $\grave{P}\acute{P}$ equation is in the standard linear form: $\mathbf{d} = \mathbf{Fm}$. This has a well-known damped least-squares Gauss-Newton solution (e.g., Gill et al., 1981): $\mathbf{m} \approx -\mathbf{H}^{-1}\mathbf{g} \approx (\mathbf{F}'\mathbf{F} + \epsilon^2)^{-1}\mathbf{F}'\mathbf{d}$, where $\mathbf{g}$ and $\mathbf{H}$ are the gradient and Hessian of E respectively, and $\mathbf{F}'$ is the adjoint operator to $\mathbf{F}$. The adjoint operator is defined by the scalar product:

$$< \mathbf{d}, \mathbf{F}\mathbf{m} > = < \mathbf{F}'\mathbf{d}, \mathbf{m} > \ . \tag{11}$$

Writing down the integral equation implied in (11), interchanging the order of integration, and taking the complex conjugate, results in an integral expression for the adjoint operator:

$$\mathbf{F}'\{\cdot\} = -\int_w \int_{\mathbf{x}_m} ik\, A_s A_r \{\cdot\} e^{-iw\tau}\, d\mathbf{x}_m\, dw \ . \tag{12}$$

In this case, the gradient can be derived as

$$\mathbf{g}(\mathbf{x};\mathbf{x}_h) = -\mathbf{F}'\mathbf{d} = \int_w \int_{\mathbf{x}_m} ik\, A_s A_r D e^{-iw\tau}\, d\mathbf{x}_m\, dw \ . \tag{13}$$

Neglecting second-derivative terms, the Hessian can be evaluated in the usual Gauss-Newton sense as:

$$\mathbf{H} = \mathbf{F}'\mathbf{F} + \epsilon^2 = \int_w \int_{\mathbf{x}_m} k A_s A_r \left[\int_{V'} k' A_s' A_r' \{1\} e^{iw\tau'}\, dV' \right] e^{-iw\tau}\, d\mathbf{x}_m\, dw + \epsilon^2(\mathbf{x};\mathbf{x}_h) \ . \tag{14}$$

This representation of the Hessian requires a complete forward modeling step as well as a complete migration step; i.e., it costs one full forward modeling of all the recorded data, plus one full prestack migration. In this form, the Hessian is spatially non-diagonal in the sense that it tries to incorporate and compensate for all point-to-point correlations of reflectivity in the subsurface. This non-diagonality should not be confused with *multi-parameter* crosscorrelations which occur in the case of acoustic or elastic parameter inversions (e.g., Beydoun and Mendes, 1989). There is only one single parameter being inverted for here: $\grave{P}\acute{P}$, and it is likely to be spatially correlated due to data bandwidth, and $\mathbf{H}$ in (14) is trying to deconvolve that spatial correlation.

In the interest of efficiency, the Hessian can be diagonalized (i.e., ignoring spatial correlations of $\grave{P}\acute{P}$), by assuming the "1" in the volume integrand of (14) is a spatially uncorrelated delta function $\delta(\mathbf{x}' - \mathbf{x})$ (e.g., Clayton and Le Bras, 1988). In this case, the diagonalized Hessian reduces to:

$$\mathbf{H} = \mathbf{F}'\mathbf{F} + \epsilon^2 \approx \int_w \int_{\mathbf{x}_m} k^2 A_s^2 A_r^2\, d\mathbf{x}_m\, dw + \epsilon^2(\mathbf{x};\mathbf{x}_h) \ . \tag{15}$$

Combining (13) and (15), results in an approximate l_2 reflectivity solution under the stationary phase condition:

$$\grave{P}\acute{P}(\mathbf{x};\mathbf{x}_h) \approx -\frac{\mathbf{g}(\mathbf{x};\mathbf{x}_h)}{\mathbf{H}(\mathbf{x};\mathbf{x}_h)} \approx \frac{-\int_w \int_{\mathbf{x}_m} ik\, A_s A_r D e^{-iw\tau}\, d\mathbf{x}_m\, dw}{\int_w \int_{\mathbf{x}_m} k^2 A_s^2 A_r^2\, d\mathbf{x}_m\, dw + \epsilon^2(\mathbf{x};\mathbf{x}_h)} \ . \tag{16}$$

The approximate diagonal Hessian solution (16) costs little more than a single conventional prestack migration in terms of floating point operations. However, one drawback is that it requires twice the memory, since the $\mathbf{g}$ and $\mathbf{H}$ images must be updated separately during the estimation (migration) process. They may only be combined as in (16) after both have been completely imaged. This seems to be the price to pay for accurate $\grave{P}\acute{P}(\Theta)$ amplitude recovery.

It should be noted that the form and weight structure of the l_2 inverse solution (16) is somewhat similar, but different in detail, to the trial solution of Bleistein (1987). In particular, (16) involves two separate but simultaneous images to be evaluated, the gradient (numerator) being a weighted Kirchhoff prestack depth migration, and the approximate Hessian (denominator) being an accumulation of the squared migration weights. Bleistein's solution involves only one migration integral since it is not a least-squares estimate, and his different migration kernel amplitude weights will give a different $\grave{P}\acute{P}$ amplitude result in general.

Reflection angles

An l_2 solution for the reflection angles Θ can be estimated directly from the reflection data D by substituting the solution (16) into the normal equation $\partial E/\partial\Theta = 0$. Unfortunately, I have not yet completed the required analysis. A difficulty arises from the fact that the kernel functions of (5) are nonlinearly related to Θ.

However, in the meantime an efficient ad hoc solution is available based on physical intuition. Consider a fixed point $\mathbf{x}$ in the subsurface. As we migrate a constant offset section into $\mathbf{x}$, the angle θ_{sr} between the source and receiver rays ranges from $\theta_{sr} \approx 0$ at $\mathbf{x}_m = \mathbf{x}_{min}$, to $\theta_{sr} \approx 2\Theta$ near the specular midpoint, and back to $\theta_{sr} \approx 0$ at $\mathbf{x}_m = \mathbf{x}_{max}$. Analogously, the differential reflection coefficient R_{PP} varies from $R_{PP} \approx 0$ (diffraction) to $R_{PP} \approx \grave{P}\acute{P}(\Theta)$ (specular reflection), to $R_{PP} \approx 0$ (diffraction) again, over the same midpoint integration range. Hence, it is apparent that R_{PP} will attain a maximal peak amplitude at the specular midpoint, whereupon $R_{PP} = \grave{P}\acute{P}(\Theta)$ and $\theta_{sr} = 2\Theta$. This physical argument suggests performing a first moment weighted estimate of Θ as follows:

$$f(2\Theta(\mathbf{x};\mathbf{x}_h)) \approx \frac{\mathbf{g}_2(\mathbf{x};\mathbf{x}_h)}{\mathbf{H}_2(\mathbf{x};\mathbf{x}_h)} \tag{17}$$

where

$$\mathbf{g}_2(\mathbf{x};\mathbf{x}_h) = \int_w \int_{\mathbf{x}_m} |k\, A_s A_r D| f(\theta_{sr}) e^{-iw\tau}\, d\mathbf{x}_m\, dw \tag{18}$$

and

$$\mathbf{H}_2(\mathbf{x};\mathbf{x}_h) = \int_w \int_{\mathbf{x}_m} |k\, A_s A_r D| e^{-iw\tau}\, d\mathbf{x}_m\, dw + \lambda^2(\mathbf{x};\mathbf{x}_h)\ , \tag{19}$$

where λ^2 is another damping parameter, and $f(\Theta)$ is a function which can be arbitrarily chosen to optimize the estimate. In practice, choosing f to be a low power of the cosine function works well, such that $f \approx \cos^{\nu}\theta_{sr}$. I use $\nu = 2$. It should be noted that the estimate (17) is very similar to the result of Bleistein (1987) for $\nu = 1$, except that the slightly different WKBJ weighting and the absolute value signs may add a certain robustness advantage, especially at subsurface points $\mathbf{x}$ where $|\grave{P}\acute{P}|$ tends to be small or zero.

Finally, the two estimates $\grave{P}\acute{P}(\mathbf{x};\mathbf{x}_h)$ and $\Theta(\mathbf{x};\mathbf{x}_h)$ can be mapped uniquely to the desired output $\grave{P}\acute{P}(\mathbf{x};\Theta)$, which completes the least-squares angle-dependent reflectivity estimation process.

SYNTHETIC DATA EXAMPLES

In this section the l_2 theory derived above is validated with two synthetic 2-D data sets. The first reflectivity model consists of five horizontal planar reflectors at depths of 1.0, 1.5, 2.0, 2.5, and 3.0 km respectively. The second reflectivity model consists of three planar reflectors which dip at 0, 15, and 30 degrees respectively. The depth of each reflector beneath the origin is 1.0, 2.0, and 3.0 km respectively. Each reflector is assigned the same angle-dependent reflectivity with the following parametric form:

$$\grave{P}\acute{P}(\Theta) = -0.26 + \sin\Theta \ , \tag{20}$$

which exhibits a strong polarity reversal at $\Theta = 15^{\circ}$ reflection angle incidence. This model AVO behavior is a challenging synthetic test in that any error in the integral formulation will easily give a wrong result, since the strong negative and positive amplitudes along a given hyperbola will not constructively interfere correctly.

The background migration velocity model is a constant 2 km/s to give analytical accuracy to the synthetic seismogram amplitudes and various ray properties. However, the sources and receivers are given directivity and the geometrical spreading is based on a typical $v(z)$ attenuation to make the synthetic amplitude more realistic.

1-D results

Figure **??** shows a representative shot gather. Realistic acquisition parameters were modeled as follows. The shot radiation pattern was modeled as $\cos\theta_s$ for a near-surface impulsive source, the receiver radiation pattern was modeled as $\cos^2\theta_r$ which emulates the receiver group and vertical component amplitude effect. The geometrical spreading was modeled proportional to $r^{-1.5}$ to simulate typical $v(z)$ spreading. Each of 120 60-fold shots were modeled with a 120-trace cable, a minimum and maximum receiver offset of 0.3 and 3.3 km, and a 25 m receiver group spacing. Total trace length is 4.0 s at a 4 ms sample interval, and the data are bandpassed to the 10-50 Hz spectral range.

Figure **??** shows the result of a standard prestack migration. The reflection amplitudes are meaningless because of the migration stacking bias along prestack hyperbolas with varying angle-dependent reflectivity amplitudes. The shallowest horizontal reflector is strongly positive due to the migration stacking bias for $\Theta > 15^{\circ}$; the recording geometry gives an illumination aperture of 10-60°. As the reflector depth increases, the recording geometry illumination aperture decreases also. This has the effect of decreasing the stacked reflector amplitudes with increasing depth, because the migration aperture stack is increasingly centered about both sides of the 15° polarity reversal, effectively summing to zero.

Figure **??** shows the l_2 estimation of $\grave{P}\acute{P}(\mathbf{x};\mathbf{x}_h)$ for a common reflection point (CRP), or "iso-x" gather. This picture is the l_2 depth-migrated equivalent of an NMO and amplitude-corrected CMP gather. Note the correct polarity reversal with increasing offset. Figure **??** is the associated $\Theta(\mathbf{x};\mathbf{x}_h)$ reflection *angle* gather. Do not be alarmed by the apparent wild variation in this figure – it is an artifact of an artificial synthetic data set which contains a very sparse set of reflections. Elsewhere in this report, I show very stable reflection angle estimates for a real data pilot study over a producing gas reservoir in the Gulf of Mexico, using this same method. Figure **??** is an overlay of the reflection angles (contoured in 5° increments), on top of the $\grave{P}\acute{P}$ estimates. Note that the 15° contour tracks the correct polarity crossing almost exactly, at each reflector depth.

Figure **??** shows the l_2 estimation of $\grave{P}\acute{P}(\Theta)$ on the $z = 1.0$ km reflector at a common reflection point (CRP). Since the model is 1-D, these figures are independent of surface location, and depend only on source-receiver offset. The l_2 estimates (crosses) closely match the correct values (dots). There is an increasing error for angles beyond about 35° which is related to spatial aliasing of the shallow migration operator impulse response. I was unsuccessful at attempts to anti-alias this operator while simultaneously preserving wide-angle reflection amplitude estimates.

Figure **??** shows a much improved l_2 estimate of $\grave{P}\acute{P}(\Theta)$ on the $z = 1.5$ km reflector. This depth is apparently below the spatial-aliasing limit, and so achieves accurate amplitude values for the entire 5-45° illumination aperture. Similarly, Figures **??** to **??** show very accurate amplitude recovery of the polarity reversal AVO curve over all recording geometry apertures. Note in particular that the l_2 nature of the inverse solution is compensating for finite recording aperture, since amplitudes are not degraded at the edges of the illumination cone (nearest and farthest angles). It is also worth mentioning that all these amplitude plots have been scaled to a single constant value. Since they all track the correct AVO curves in an absolute sense, the relative amplitude recovery from reflector to reflector, as well as in angle along a given reflector, is correct. Finally, note how the illumination aperture narrows from about 10-60° at 1 km depth, down to 5-25° at 3 km depth.

In summary, the l_2 theory derived here accurately estimates the theoretical angle-dependent reflectivity function for a 1-D reflector model in the presence of source/receiver radiation patterns, geometric spreading, high-frequency Q attenuation (not shown here), and limited data acquisition aperture. It may be worth noting that the socalled “2.5-D” amplitude correction to the recorded data is not required in the l_2 formulation, since data missing from the y-direction is just another form of finite recording aperture. However, the associated $\pi/4$ phase shift is required, since phase does not seem to be properly taken into account in the l_2 energy norm.

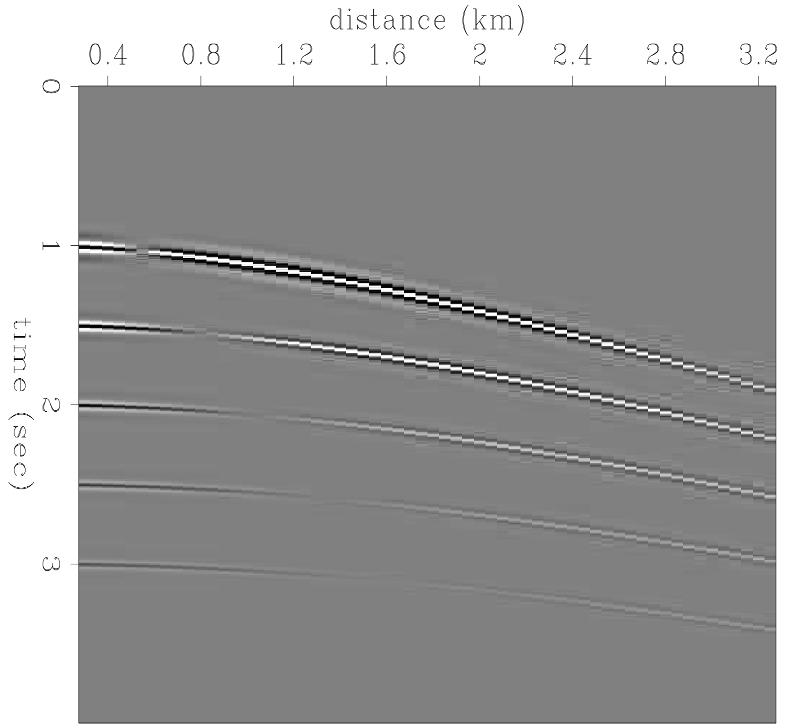

Figure 2: Synthetic shot gather for five horizontal reflectors. david2-flat-shot [CR]

2-D results

Realistic acquisition parameters were modeled as in the 1-D example. The shot radiation pattern was modeled as $\cos\theta_s$ for a near-surface impulsive source, the receiver radiation pattern was modeled as $\cos^2\theta_r$ to emulate the receiver group and vertical component amplitude effect. The geometrical spreading was modeled proportional to $r^{-1.5}$ to simulate typical $v(z)$ spreading. Each of 240 60-fold shots were modeled with a 120-trace cable, a minimum and maximum receiver offset of 0.3 and 3.3 km, and a 25 m receiver group spacing. Total trace length is 6.0 s at a 4 ms sample interval, and the data are bandpassed to the 10-50 Hz spectral range. Twice the number of shots and 2 extra seconds of recording time were required to capture the 30 degree dipping event in a comparative manner to the 1-D recording geometry.

Figure **??** shows a representative shot gather. Note the crossing of events due to structural dip at the far offsets. This far offset event mixing is expected to cause some amplitude estimation problems, since the events never completely decouple. Figure **??** shows the result of a standard prestack migration. The reflection amplitudes are meaningless because of the migration stacking bias along prestack hyperbolas with

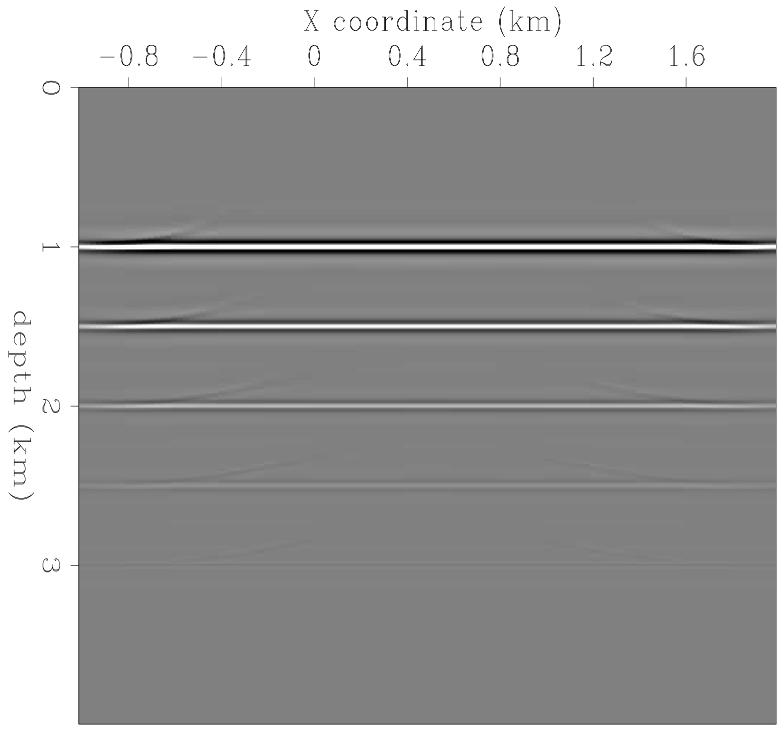

Figure 3: Standard prestack migration and stack. Reflection amplitudes are meaningless due to migration stack bias along hyperbolic prestack angle-dependent reflectivity variation. david2-flat-mig [CR]

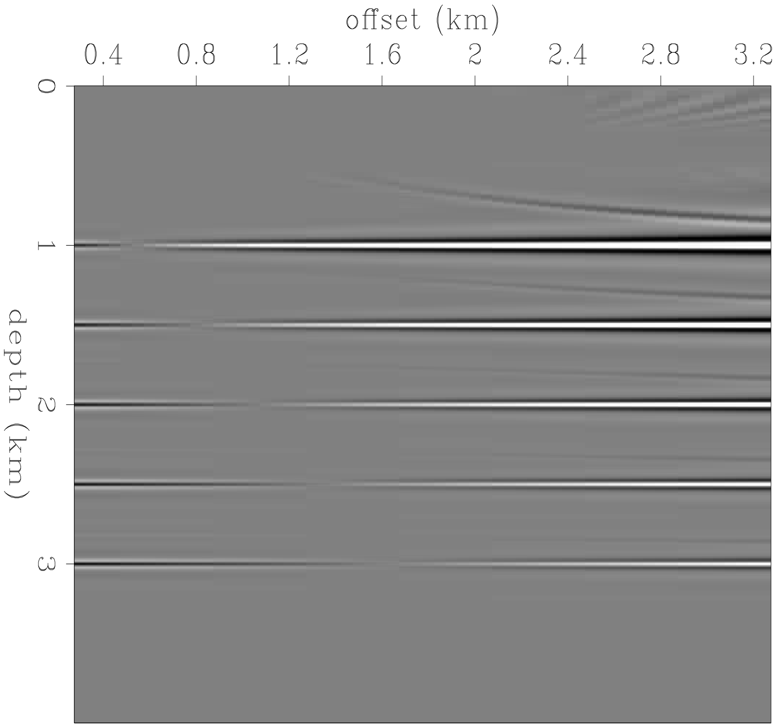

Figure 4: Migrated estimate of $\grave{P}\acute{P}(\mathbf{x};\mathbf{x}_h)$ at a CRP or “iso-x” gather. Note correct AVO polarity reversal with offset. $\boxed{\text{david2-flat-Rcrp}}$ [CR]

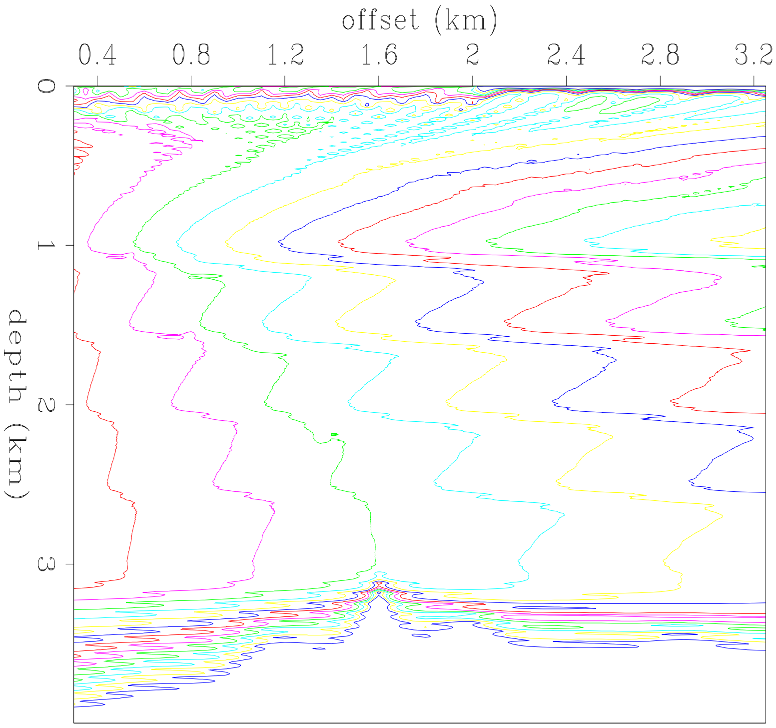

Figure 5: Migrated reflection angle estimates of $\Theta(\mathbf{x};\mathbf{x}_h)$ for a CRP gather, contoured in 5° increments. $\boxed{\text{david2-flat-Tcrp}}$ [CR]

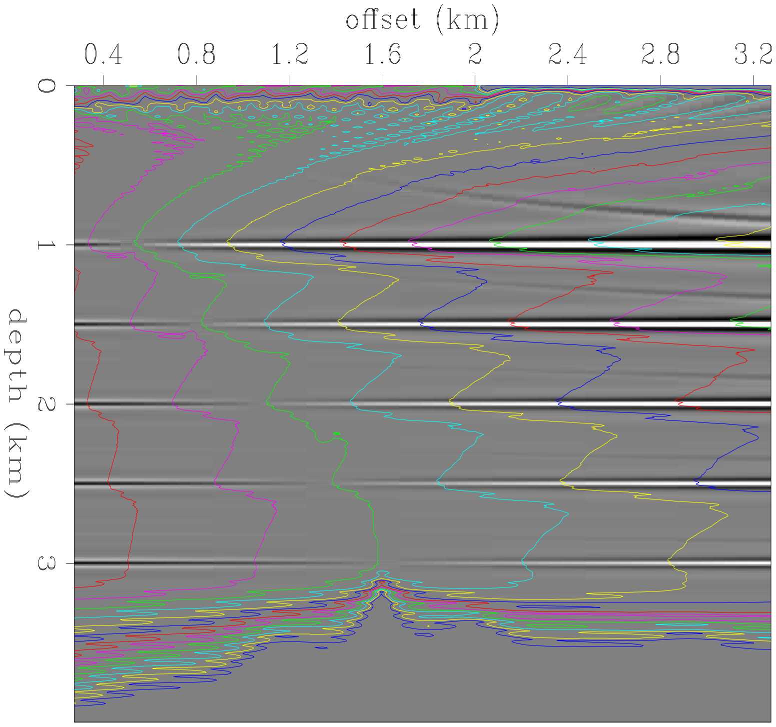

Figure 6: Overlay of $\Theta(\mathbf{x};\mathbf{x}_h)$ on $\grave{P}\acute{P}(\mathbf{x};\mathbf{x}_h)$. $\boxed{\text{david2-flat-RTcrp}}$ [CR]

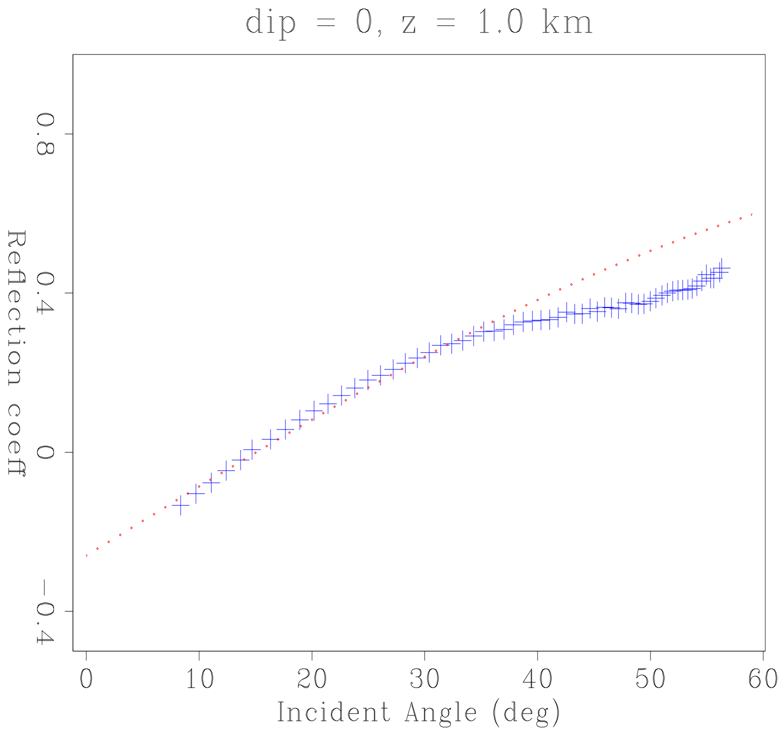

Figure 7: $\grave{P}\acute{P}(\Theta)$ recovery on the horizontal reflector at 1.0 km depth. $\boxed{\text{david2-flat1-rth}}$ [CR]

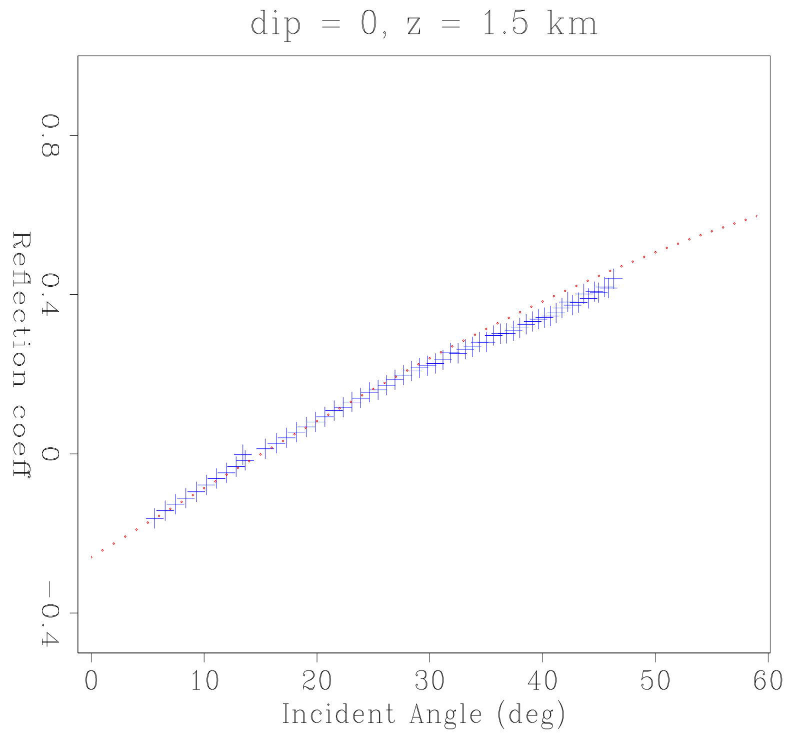

Figure 8: $\grave{P}\acute{P}(\Theta)$ recovery on the horizontal reflector at 1.5 km depth. $\boxed{\text{david2-flat2-rth}}$ [CR]

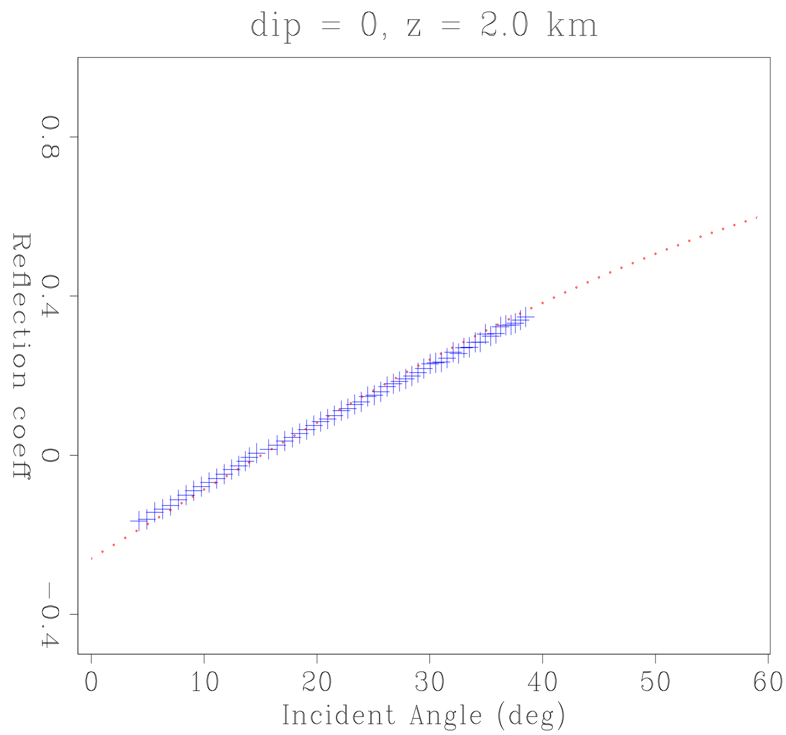

Figure 9: $\grave{P}\acute{P}(\Theta)$ recovery on the horizontal reflector at 2.0 km depth. $\boxed{\text{david2-flat3-rth}}$ [CR]

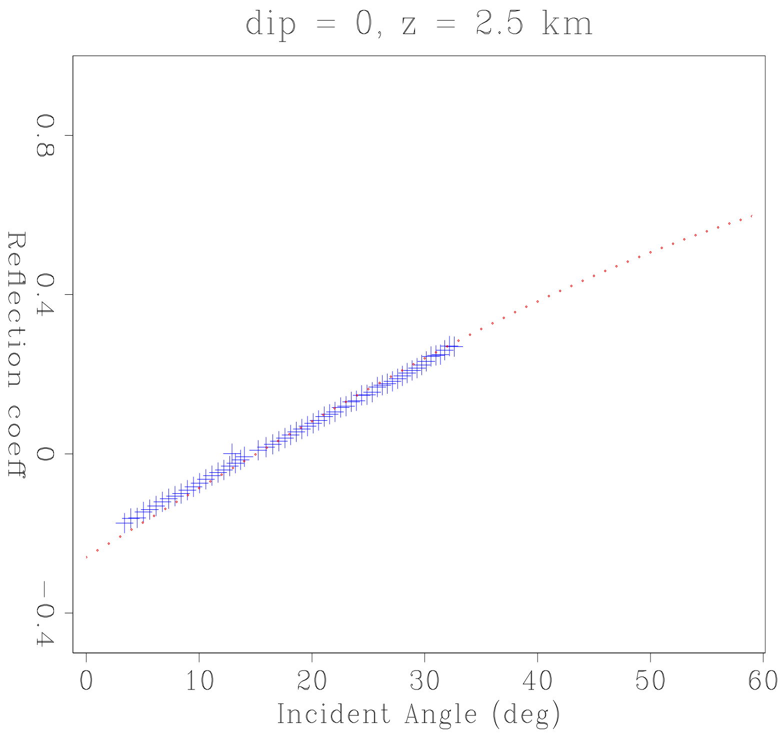

Figure 10: $\grave{P}\acute{P}(\Theta)$ recovery on the horizontal reflector at 2.5 km depth. david2-flat4-rth [CR]

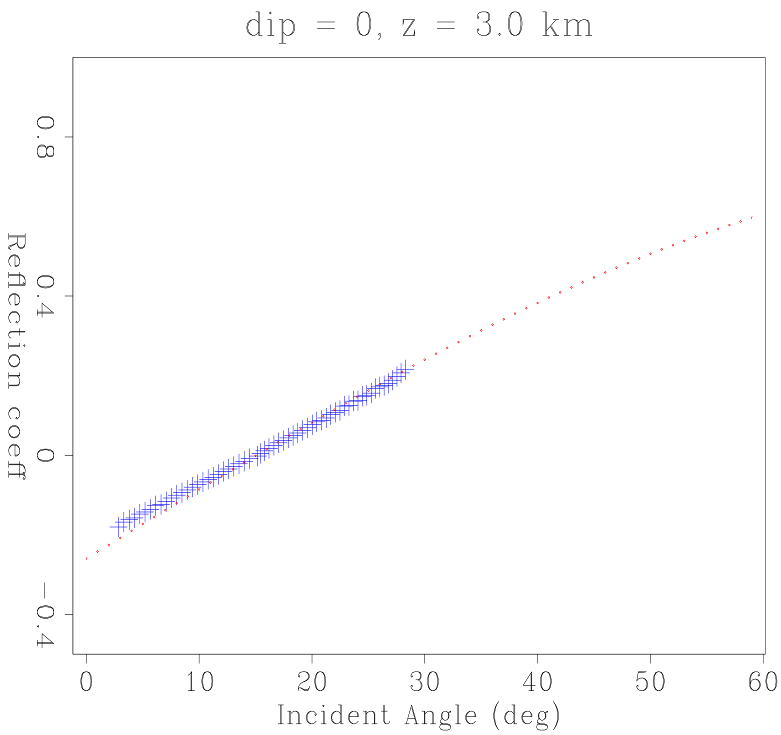

Figure 11: $\grave{P}\acute{P}(\Theta)$ recovery on the horizontal reflector at 3.0 km depth. david2-flat5-rth [CR]

varying angle-dependent reflectivity amplitudes, and varying data aperture with dip. In fact, the horizontal reflector is strongly positive due to the migration stacking bias for $\Theta > 15^\circ$, and the 30° dipping event is actually negative due to the data aperture bias at reflection angles less than 15°.

Figure **??** shows the l_2 estimation of $\grave{P}\acute{P}(\mathbf{x};\mathbf{x}_h)$ for a common reflection point (CRP), or "iso-x" gather. This picture is the l_2 depth-migrated equivalent of an DMO/NMO and amplitude-corrected CMP gather. Note the correct polarity reversal with increasing offset. This time, however, the 2-D dipping structure has caused the polarity crossing to be skewed to far offsets at depth, in contrast to the 1-D CRP of Figure **??**. That is because far offset geometries tend to move the reflection point up dip on a dipping reflector, and narrow the aperture angle.

Figure **??** is the associated $\Theta(\mathbf{x};\mathbf{x}_h)$ reflection *angle* gather. Figure **??** is an overlay of the reflection angles (contoured in 5° increments), on top of the $\grave{P}\acute{P}$ estimates. Note that the 15° contour tracks the correct polarity crossing almost exactly, at each reflector depth, even though there is significant skew due to dip, especially on the 30° dip at 3.0 km depth.

Figure **??** shows the amplitude recovery with angle on the shallow horizontal reflector at 1.0 km depth. This is an interesting picture that can teach us a lot about practical amplitude recovery. At first, I thought that this plot should look identical to Figure **??**, since they are both horizontal reflectors at 1.0 km depth. However, several factors come into play to degrade the far offset amplitude recovery. The first is spatial aliasing of the migration operator *from the deeper, dipping reflections*. As the dip increases, the spatial aliasing gets worse, and those aliased-operator artifacts can cause significant destructive interference and amplitude contamination on a completely different reflector (i.e., the shallow horizontal reflector). Second, the dip on the 15° and 30° events causes the three hyperbolas to overlap each other at far offsets (see Figure **??**). If you run a movie of all the shot gathers, you see that these three events never really decouple themselves very well at any point along the line. That means there is no easy way to distinguish their respective amplitude contributions at far offsets, and therefore the far offset amplitude estimates will be significantly in error. This effect would not be seen in a synthetic test involving only one dipping reflector, or non-overlapping reflection hyperbolas. This result provokes some sobering thoughts regarding the implications for AVO in 2-D dip structure using standard offset cables lengths.

As the dip increases, the illumination aperture narrows, and the amplitude estimate gets better because of the increased redundancy in the least-squares summation estimate. Also the effects of operator aliasing decrease with depth of target and smaller illumination angles. Figure **??** shows reasonably good amplitude and angle estimation up to 30°, and Figure **??** shows excellent amplitude recovery on the 30° dipping event. Note that the range of Θ illumination on the deeper dipping reflector (2–22°) is much less than the shallower horizontal reflector (5–45°), as expected.

CONCLUSIONS

I have developed and implemented a least-squares theory that makes robust estimates of the angle-dependent reflectivity $\grave{P}\acute{P}(\Theta)$ from recorded surface seismic reflection data. Both angles and reflection coefficients are estimated directly from the data without a priori knowledge of the subsurface structural dip. The implementational cost of this approach is little more than a standard Kirchhoff prestack migration. The method naturally allows compensation for source/receiver directivity, geometric spreading, transmission loss, high-frequency Q attenuation, and limited data acquisition aperture. Synthetic tests show good to excellent results on a 1-D and 2-D model with up to 30° of structural dip. However, amplitude artifacts and errors can be magnified by dipping structure due to increased spatial aliasing of the migration operator, and hyperbolic event interference and coupling at the far offsets.

ACKNOWLEDGMENTS

I would like to thank Wafik Beydoun (Elf Research UK) for his challenging comments and ongoing enthusiasm in this work. Additionally, Norm Bleistein (Colorado School of Mines) and Sam Gray (Amoco Research) provided helpful comments. Patrick Blondel and Matthias Schwab provided very careful reviews which improved the paper.

REFERENCES

Aki, K., and Richards, P. G., 1980, Quantitative seismology: W. H. Freeman and Company.

Beydoun, W. B., and Mendes, M., 1989, Elastic ray-Born l-2 migration/inversion: Geophys. J., **97**, 151–160.

Beylkin, G., 1985, Imaging of discontinuities in the inverse scattering problem by inversion of a causal generalized Radon transform: J. Math. Phys., **26**, 99–108.

Bleistein, N., 1987, On the imaging of reflectors in the earth: Geophysics, **52**, 931–942.

Cunha Filho, C., 1992, Elastic modeling and migration in earth models: Ph.D. thesis, Stanford University.

de Bruin, C., 1992, Linear AVO inversion by prestack depth migration: Ph.D. thesis, Delft University, The Netherlands.

Frazer, L. N., and Sen, M. K., 1985, Kirchhoff-Helmholtz reflection seismograms in a laterally inhomogeneous multi-layered elastic medium – I. Theory: Geophys. J. R. Astr. Soc., **80**, 121–147.

Gill, P. E., Murray, W., and Wright, M. H., 1981, Practical optimization: Academic Press, Inc.

Goodman, J. W., 1968, Introduction to Fourier optics: McGraw-Hill.

Le Bras, R., and Clayton, R. W., 1988, An iterative inversion of back-scattered acoustic waves: Geophysics, **53**, 501–508.

Lumley, D. E., and Beydoun, W. B., 1991, Elastic parameter estimation by Kirchhoff prestack depth migration/inversion: Stanford Exploration Project Report, **70**, Stanford University, 165–192.

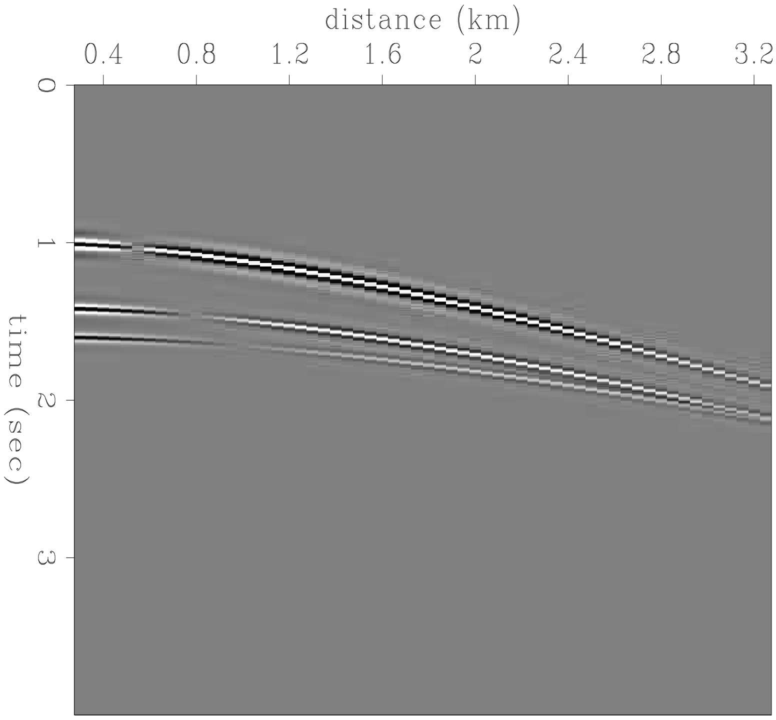

Figure 12: Synthetic shot gather for three reflectors having 0, 15, and 30 degrees dip respectively. david2-dips-shot [CR]

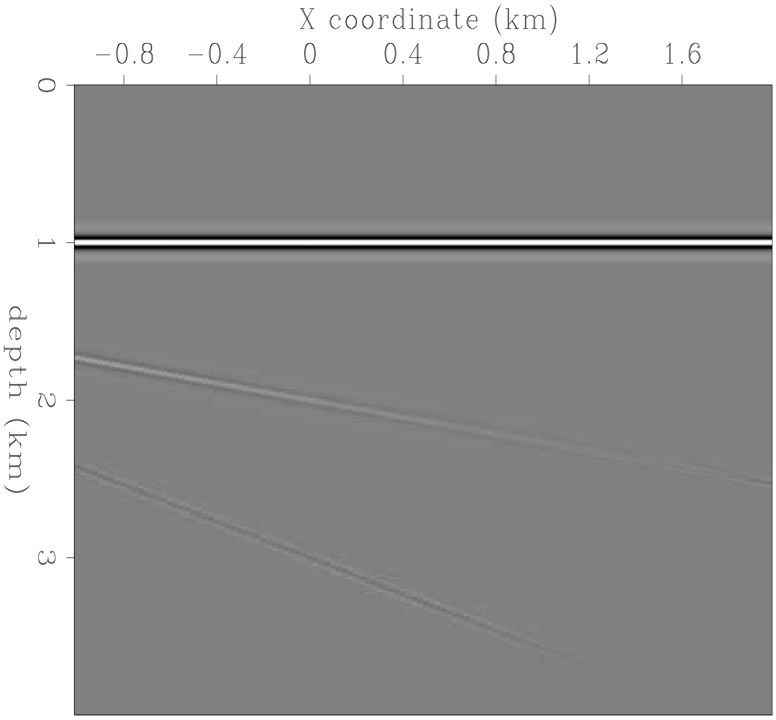

Figure 13: Standard prestack migration and stack. Reflection amplitudes are meaningless due to migration stack bias along hyperbolic prestack angle-dependent reflectivity variation. david2-dips-mig [CR]

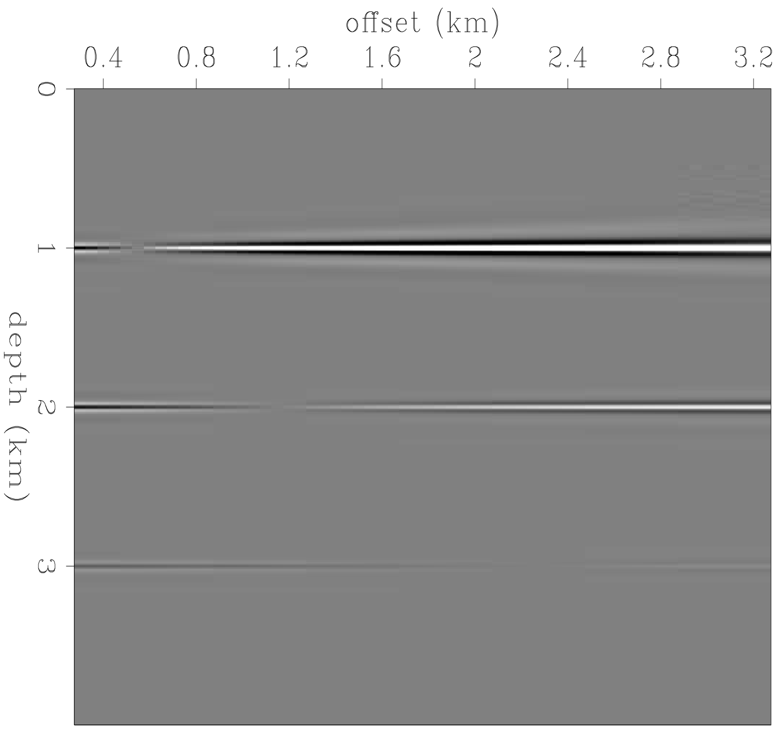

Figure 14: Migrated estimate of $\grave{P}\acute{P}(\mathbf{x};\mathbf{x}_h)$ at a CRP or "iso-x" gather. Note correct AVO polarity reversal with offset. $\boxed{\text{david2-dips-Rcrp}}$ [CR]

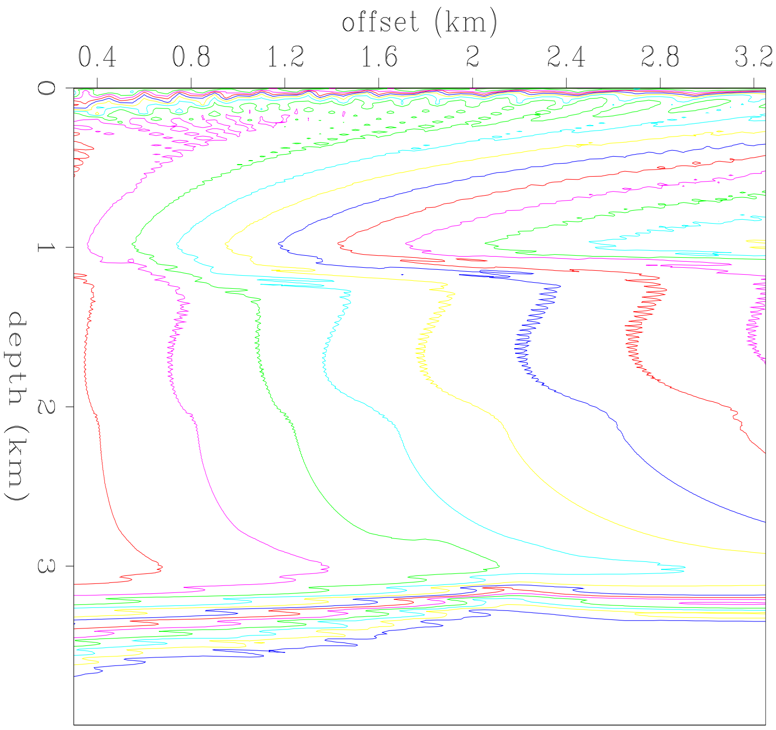

Figure 15: Migrated reflection angle estimates of $\Theta(\mathbf{x};\mathbf{x}_h)$ for a CRP gather, contoured in 5° increments. $\boxed{\text{david2-dips-Tcrp}}$ [CR]

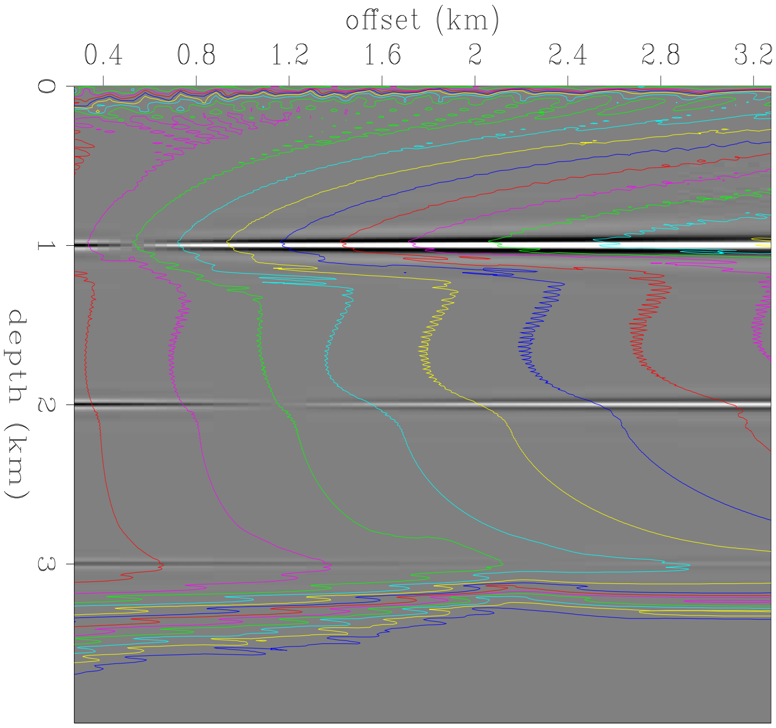

Figure 16: Overlay of $\Theta(\mathbf{x};\mathbf{x}_h)$ on $\grave{P}\acute{P}(\mathbf{x};\mathbf{x}_h)$. david2-dips-RTcrp [CR]

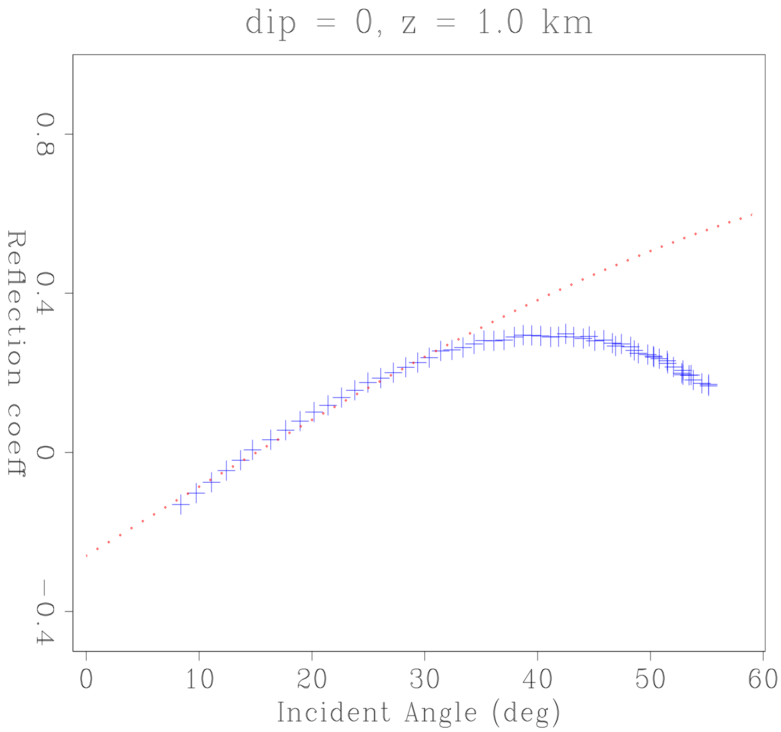

Figure 17: $\grave{P}\acute{P}(\Theta)$ recovery on the horizontal reflector at 1.0 km depth. david2-dips1-rth [CR]

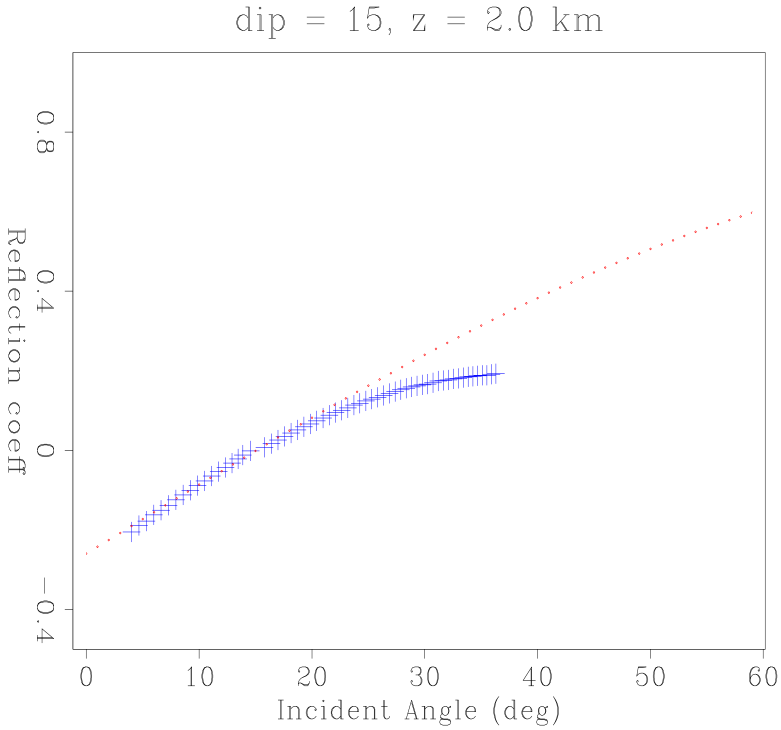

Figure 18: $\grave{P}\acute{P}(\Theta)$ recovery on the 15° dipping reflector at 2.0 km depth below the origin. david2-dips2-rth [CR]

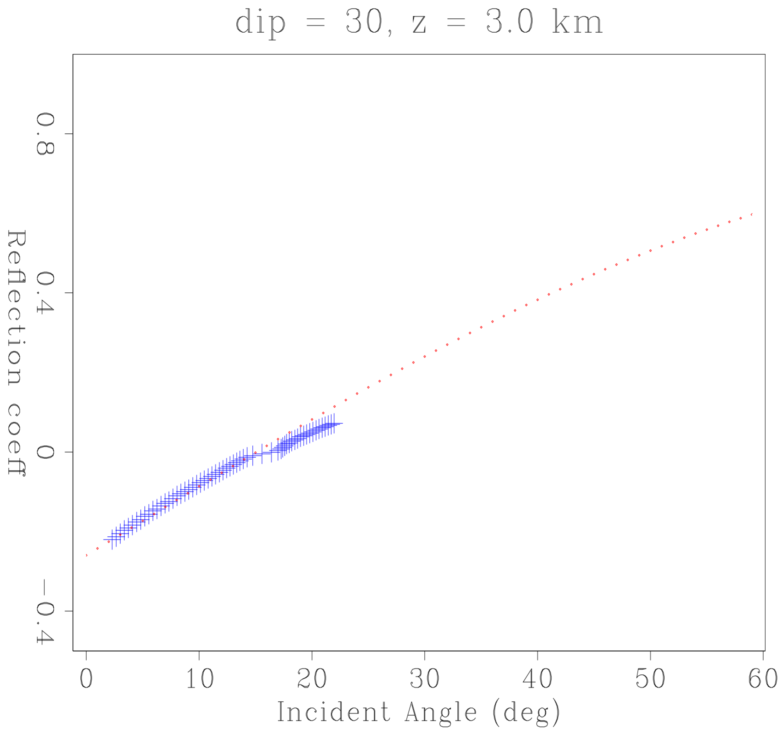

Figure 19: $\grave{P}\acute{P}(\Theta)$ recovery on the 30° dipping reflector at 3.0 km depth below the origin. david2-dips3-rth [CR]